

Impact of ionosphere on InSAR observation and coseismic slip inversion: Improved slip model for the 2010 Maule, Chile, earthquake



Bochen Zhang^{a,b,c}, Xiaoli Ding^{c,*}, Falk Amelung^d, Chisheng Wang^{a,e}, Wenbin Xu^{f,g}, Wu Zhu^h, Masanobu Shimadaⁱ, Qingjun Zhang^j, Toshitaka Baba^k

^a MNR Key Laboratory for Geo-Environmental Monitoring of Great Bay Area & Guangdong Key Laboratory of Urban Informatics & Shenzhen Key Laboratory of Spatial Smart Sensing and Services, Shenzhen University, 518060 Shenzhen, China

^b College of Civil and Transportation Engineering, Shenzhen University, 518060 Shenzhen, China

^c Department of Land Surveying and Geo-Informatics, The Hong Kong Polytechnic University, Kowloon, Hong Kong, China

^d Department of Marine and Geosciences, Rosenstiel School of Marine and Atmospheric Sciences, University of Miami, Miami, Florida, USA

^e School of Architecture & Urban Planning, Shenzhen University, 518060 Shenzhen, China

^f Laboratory of Radar Remote Sensing, School of Geosciences and Info-Physics, Central South University, Changsha 410083, China

^g Key Laboratory of Metallogenic Prediction of Nonferrous Metals and Geological Environment Monitoring, Central South University, 410083 Changsha, China

^h School of Geology Engineering and Geomatics, Chang'an University, Xi'an, Shaanxi, China

ⁱ School of Science and Engineering, Tokyo Denki University, 350-0394 Saitama, Japan

^j Beijing Institute of Spacecraft System Engineering, China Academy of Space Technology, Beijing 100094, China

^k Graduate School of Science and Technology, Tokushima University, Tokushima, Japan

ARTICLE INFO

Editor: Jing M. Chen

Keywords:

2010 Maule earthquake

InSAR

Ionospheric artifacts

Fault slip model

Slip-to-trench rupture

ABSTRACT

Satellite synthetic aperture radar (SAR) signals are affected by the Earth's ionosphere when the signals travel through the ionosphere. We first analyze the impact of ionospheric variation on the coseismic deformation results derived from interferometric SAR (InSAR) for the 2010 Maule, Chile, earthquake. We then jointly invert leveling, GPS and InSAR data for the coseismic slip distribution. The bias in the inverted slip distribution caused by the ionospheric variation is especially investigated. Our results show that mitigating the effect of ionospheric artifacts on long wavelengths, such as the L-band, InSAR data is critical to studying some strong earthquakes. It is therefore advisable at least as a precaution to check the level of significance of the ionospheric artifacts when studying strong earthquakes with InSAR, and when the artifacts are found to be significant, corrections for the artifacts should be applied. This research also indicates that megathrust rupturing occurred mainly at two asperities with peak slip magnitudes reaching 15.7 m and 9.8 m. More importantly, generally unlike the common existing understanding, our results show that the rupture reached the trench only in the northern segment of the trench (near 34.9°S–35.4°S).

1. Introduction

On February 27, 2010, the Maule, Chile, earthquake (Mw 8.8) ruptured the Nazca-South America subduction zone offshore of the southern-central Andes. The epicenter of the earthquake was within the rupture zone (known as the Darwin gap or Constitución gap) of the 1835 Concepción earthquake (Mw 8.5), north of the epicenter of the 1960 Valdivia earthquake (Mw 9.5) and south of the epicenter of the 1928 Talca earthquake (Mw 8.0) (Campos et al., 2002). The earthquake correlated highly with the preseismic locking of the Constitución gap (Moreno et al., 2010), where approximately 11–14 m of slip deficit had

accumulated since 1835 under the assumption that the interplate locking was 100% with a convergent motion of 63–80 mm/yr (Lay et al., 2010; Pollitz et al., 2011). The 2010 rupture resulted in significant displacements as measured by geodetic observations, including those of the Global Positioning System (GPS), leveling and interferometric synthetic aperture radar (InSAR) (Farías et al., 2010; Tong et al., 2010; Vigny et al., 2011). Research based on observations and seismic and tsunami data has suggested that the rupture extended approximately 500 to 600 km along strike and was dominated by downdip slip (Delouis et al., 2010; Hayes et al., 2013; Lay et al., 2010; Lin et al., 2013; Lorito et al., 2011; Moreno et al., 2012; Pollitz et al., 2011; Tong et al., 2010;

* Corresponding author.

E-mail address: xl.ding@polyu.edu.hk (X. Ding).

Vigny et al., 2011; Yue et al., 2014). The coseismic slip was concentrated at two major asperities, one located north-northeast of the hypocenter and the other south of the hypocenter, with maximum slips of 15 to 21 m. The slip models presented in previous studies vary considerably due to differences in the data, fault geometries, and data inversion strategies adopted (Lin et al., 2013; Moreno et al., 2012; Yue et al., 2014).

InSAR data are advantageous for studying megathrust faults due to the extensive spatial coverage and high spatial resolution of the data (Delouis et al., 2010; Hayes et al., 2014; Xu, 2017). InSAR data are, however, often affected by various errors, such as inaccurate satellite orbit information and varying atmospheric delays (Ding et al., 2008; Feng and Jónsson, 2012; Liang et al., 2018; Scott and Lohman, 2016; Yu et al., 2018; Zhang et al., 2016).

The ionosphere, a layer at altitudes of 75–1000 km above the Earth's surface, is a dynamic and dispersive medium. As electromagnetic waves travel through the ionosphere, they interact with free ions, causing path delay and polarization plane rotation of the SAR signal. Variations in the electron density within the ionosphere produce changes in the signal prorogation time, and the ionospheric phase shift leads to difficulties in retrieving the deformation phase from InSAR data. Moreover, ionospheric perturbations and scintillations may introduce other effects, such as pixel shifting of the image, degradation of the image resolution, and defocusing of the image (Xu et al., 2004). InSAR data, especially data from low-frequency SAR systems such as the Advanced Land Observing Satellite (ALOS) Phased Array L-band Synthetic Aperture Radar (PALSAR), can be affected significantly by ionospheric variations (Fattah et al., 2017; Feng and Jónsson, 2012; Gomba et al., 2016; Gray et al., 2000; Meyer et al., 2006; Zhang et al., 2016; Zhang et al., 2018). The signature of seismic ionospheric perturbation was observed for the Maule earthquake by Galvan et al. (2011) with GPS observations. Tong et al. (2010) and Lin et al. (2013) indicated that some of the ALOS PALSAR data previously used to study the Maule earthquake may have been affected by ionospheric perturbation. The effect of ionospheric perturbations, however, has not been studied.

In this paper, we first analyze and correct the ionospheric contributions to the InSAR data acquired over the rupture region of the 2010 Maule earthquake. We then determine the effects of ionospheric variation on the InSAR and the fault slip inversion of the earthquake. The novelty of the study is summarized as follows: (1) the impacts of ionospheric artifacts on coseismic slip models are investigated thoroughly taking the 2010 Maule earthquake as an example; (2) the new fault slip model for the 2010 Maule earthquake shows that the rupture reached the trench only in the northern segment of the trench (near 34.9°S–35.4°S); (3) from a scientific perspective, it is advisable to check the level of significance of ionospheric artifacts in InSAR observations when studying earthquakes similar to the case presented in this study.

2. Data and method

2.1. InSAR data processing

ALOS PALSAR (L-band) data from nine adjacent ascending tracks (Stripmap mode) and one descending track (ScanSAR mode) (Fig. 1 and Table 1) are adopted to compute the coseismic displacements of the 2010 Maule earthquake. The interferometric SAR pairs shown in Supplementary Fig. S1 are used to generate coseismic displacement interferograms. Single look complex (SLC) images are first formed from raw SAR data (level 1.0 product). To mitigate the effect of slow changes in the Doppler bandwidth caused by an operational issue with the SAR sensor, the system periodically (approximately every 2000 km of ground track) changes the pulse repetition frequency (PRF) of the transmitted signal (Shimada and Ohtaki, 2010). Difficulties are therefore encountered when processing long-strip images (such as ascending tracks p111 and p112; see Fig. 1). The ALOS PALSAR data are provided as individual frames. The overlapping region is used for concatenating two adjacent frames along the same track. For the ascending tracks, we concatenate

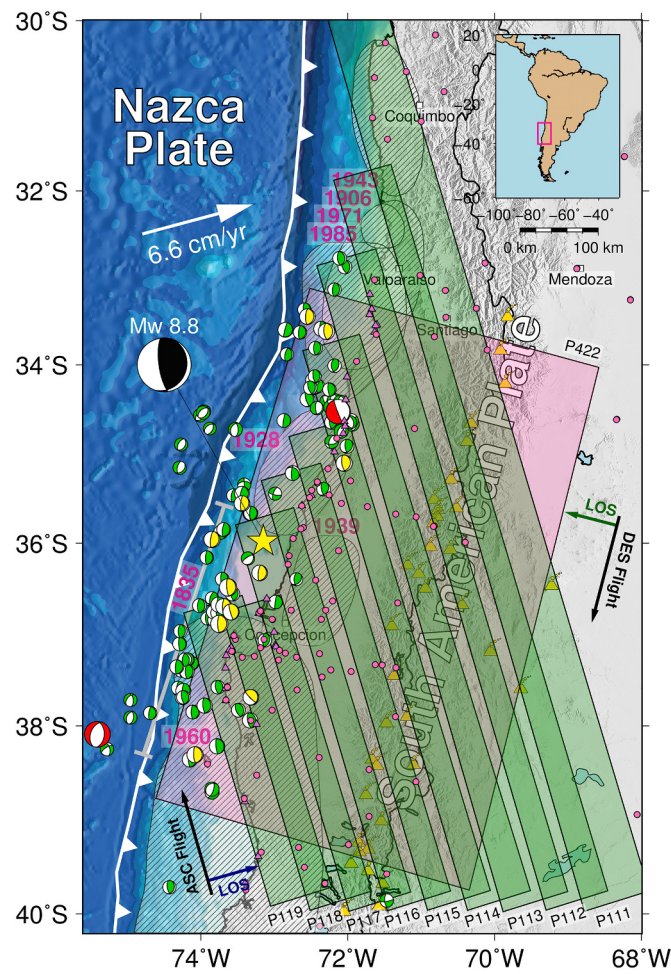


Fig. 1. Location map of the 2010 Maule megathrust earthquake. The star symbol marks the epicenter of the main shock according to the USGS. Aftershocks within the first three months of the main shock (according to the Global Centroid Moment Tensor (GCMT) catalog) are represented by the beach ball symbols, where shocks of $Mw > 4.5$ are shown in green, $Mw > 6$ in yellow, and $Mw > 7$ in red. The white boundary line between the Nazca and South American plates is from (Bird, 2003). The gray line and shaded areas show the rupture zones of earthquakes between 1835 and 1960 (Beck et al., 1998; Campos et al., 2002; Delouis et al., 2010; Moreno et al., 2009). The dots and triangles denote the locations of leveling benchmarks and GPS stations, respectively. The rectangular areas in green and pink outline the coverage of the ascending and descending InSAR data, respectively. (For interpretation of the references to colour in this figure legend, the reader is referred to the web version of this article.)

the raw data with the same PRF values. Prior to the interferometric processing of the ScanSAR data from the descending track, we synchronize the individual burst images in the azimuth direction (Bamler and Eineder, 1996) to ensure that the Doppler spectra completely overlap, thereby improving the interferometric coherence. Synchronization of the ScanSAR azimuth bursts is achieved by obtaining the burst overlap with the time information and then filtering the raw data in azimuth to retain only the overlapping segments of each burst. The topographic phase in InSAR data is estimated and subtracted using a three-arc-second digital elevation model (DEM) from the Shuttle Radar Topography Mission (SRTM) (Farr and Kobrick, 2000). Precision orbital data are applied to estimate the offsets of the imaging geometry and eliminate the orbital fringes. We then use adaptive filtering to reduce the noise of the interferometric phase and improve the performance of phase unwrapping (Goldstein and Werner, 1998). Finally, we determine the absolute coseismic displacement by unwrapping the obtained

Table 1
SAR images used.

Track	Frame	Master		Slave		Modes of SAR Data	B_p^a (m)	Flight Direction
		PRF (Hz)	Date	PRF (Hz)	Date			
111	6380–6450	2100.84	2007/10/12	2123.14	2010/03/04	FBD ^b -FBS ^c	-275.2	Ascending
	6460–6570	2132.20		2123.14			-261.8	
112	6380–6430	2114.16	2010/02/03	2100.84	2010/03/21	FBS-FBS	-545.6	
	6440–6530	2114.16		2127.66			-506.1	
113	6380–6510	2114.16	2008/02/15	2123.14	2010/04/07	FBS-FBS	294.8	
114	6380–6430	2100.84	2007/07/17	2118.64	2010/03/09	FBD-FBS	-686.5	
	6440–6450	2114.16	2008/04/18	2114.16	2010/04/24	FBS-FBS	828.0	
	6460–6490	2118.64	2010/01/22	2118.64	2010/03/09	FBS-FBS	-304.9	
115	6380–6470	2123.14	2010/02/08	2100.84	2010/03/26	FBS-FBS	-455.4	
116	6380–6460	2114.16	2010/02/25	2109.70	2010/04/12	FBS-FBS	-522.7	
117	6380–6450	2105.26	2009/03/11	2109.70	2010/03/14	FBS-FBS	170.8	
118	6380–6430	2109.70	2010/02/13	2123.14	2010/03/31	FBS-FBS	-770.4	
119	6380–6430	2114.16	2010/01/15	2123.14	2010/03/02	FBS-FBS	-483.7	
422	4300–4400	2150.54	2008/04/10	2150.54	2010/03/01	ScanSAR-ScanSAR	1630.1	Descending

^a Perpendicular baseline.

^b FBD: fine-beam dual polarization mode of ALOS PALSAR data.

^c FBS: fine-beam single polarization mode.

displacement interferograms with the minimum cost flow (MCF) algorithm (Chen and Zebker, 2001) and adjust the unwrapped interferograms to the GPS measurements (Moreno et al., 2012; Tong et al., 2010; Vigny et al., 2011). For the southern parts of tracks p111, p112, and p114 where there are no GPS stations, the coseismic displacements are determined based on InSAR-derived displacements with a tie-point in the overlapping region along the same track.

2.2. Correction for ionospheric effect on InSAR data

To quantify the effect of ionospheric variation on the ascending SAR data, we first calculate the ground displacement in the azimuth direction (hereafter referred to as azimuth displacement) using the multiple aperture interferometry (MAI) technique (Barbot et al., 2008; Bechor and Zebker, 2006; Jung et al., 2009) (Fig. 2). Variations in the total electron content (TEC) in the ionosphere between two SAR acquisitions

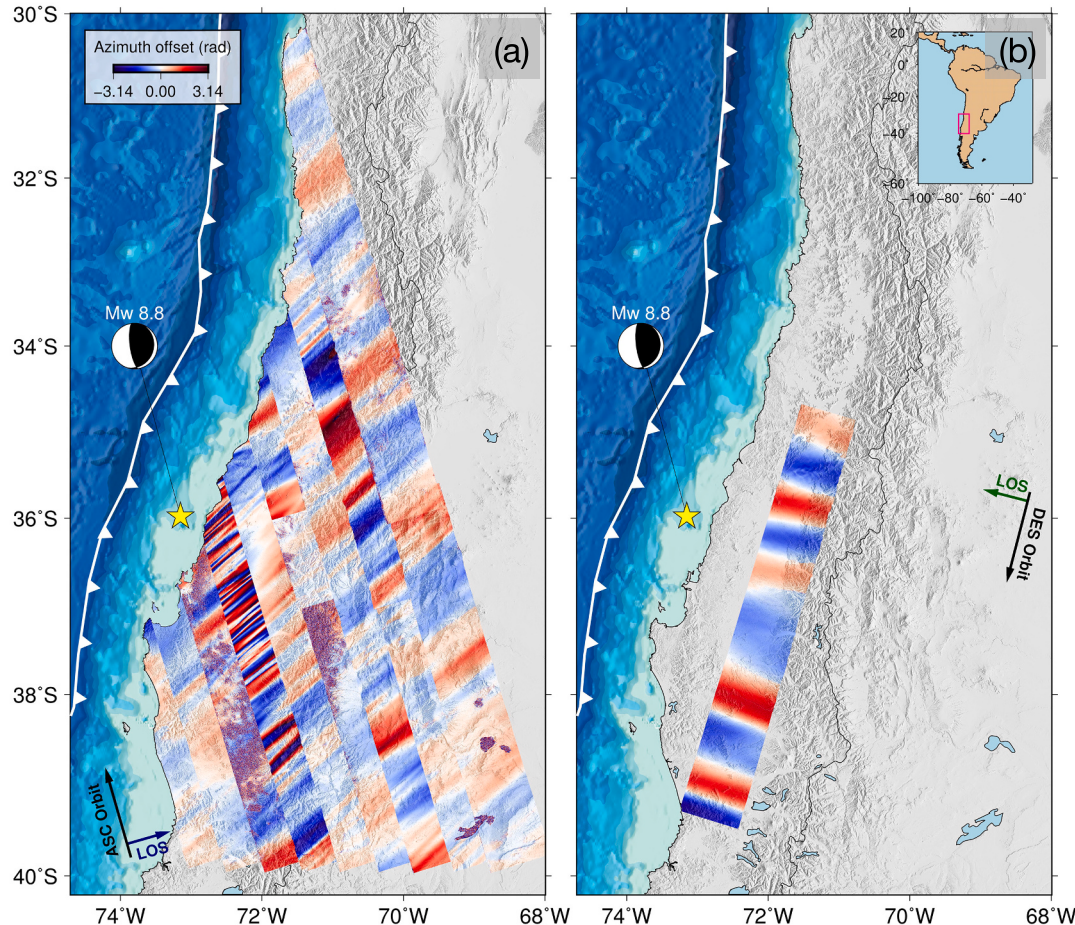


Fig. 2. Azimuth displacement from (a) ascending InSAR data and (b) track 420 of descending InSAR data (Tong et al., 2010). Both results clearly show ionospheric variations along with radar flight directions.

shift the pixel positions in the SAR images in the azimuth direction. Accurate coregistration of the SAR images is then carried out (Chen and Zebker, 2014) to correct the pixel shifts (exceeding a resolution cell) in the interferograms and to enhance the coherence. A pair of bandpass filters is then used to divide the full range spectrum of the inversely focused SAR signal into two subbands corresponding to two different central frequencies using a Fourier transform (Gomba et al., 2016; Rosen et al., 2010) in conjunction with quadrature demodulation to compensate for the phase change due to the central frequency shift (Cumming and Wong, 2005). Subband SLC images are constructed to generate low-band and high-band interferograms. The ionosphere is a dispersive medium in which electromagnetic waves travel at different velocities depending on their frequency. Therefore, the ionospheric phase component (ionospheric phase screen (IPS)) is the only phase term related to radar frequency and can be separated from nondispersive phase components (such as those related to deformation, atmosphere, and orbital errors) (Gomba et al., 2016). Finally, we use a median absolute deviation (MAD) filter (Leys et al., 2013) to eliminate outliers in the IPS and a weighted Gaussian filter to produce the final IPS to correct the full-band interferogram. The ionospheric corrections are performed using a self-alone module that we developed for GAMMA software (version 20151209), as in (Zhang et al., 2018). To the best of our knowledge, the functions of ionospheric correction are currently partially or fully integrated in some InSAR processing software, such GAMMA, ISCE and GMTSAR.

2.3. Slip modeling

We divide the fault plane into 4200 quadrangular patches, each with a size of 5×5 km, with an overall dip length of 175 km and strike length of 600 km (Bird, 2003). The depth and dip angle of each patch were sampled from the United States Geological Survey (USGS) Slab2.0 model (Hayes et al., 2018) (Supplementary Fig. S2). The rake angles are constrained to 80° to 120° in the inversion according to the focal mechanisms and tectonic setting. The InSAR data are downsampled to 8505 and 4016 points for the ascending and descending tracks, respectively, by block median averaging with a grid size of $0.05^\circ \times 0.1^\circ$ (latitude \times longitude), following the same approach as (Tong et al., 2010). The main reason for choosing to use uniform data subsampling is to keep the locations of the sampled data points before and after the ionospheric corrections the same. A denser sample near the rupture zone can result if the subsampling is performed based on the gradient of the line-of-sight (LOS) displacements (Wang and Fialko, 2018), but the locations of the sampled data will be changed. In the joint inversion, we combine the displacements (in the east, north, and up directions) from 170 continuous and campaign GPS sites as in (Moreno et al., 2012; Tong et al., 2010; Vigny et al., 2011) and those from 34 leveling benchmarks as in (Farías et al., 2010). The spatial distributions of the leveling and GPS data are denoted by dots and triangles, respectively, in Fig. 1. Details of the temporal distributions of these data can be found in (Farías et al., 2010; Moreno et al., 2012; Tong et al., 2010; Vigny et al., 2011). Green's functions corresponding to each of the datasets are computed in a homogeneous elastic half-space with a Poisson's ratio of 0.25 using Okada's formulas (Okada, 1985), representing a rectangular analytical source model that is commonly used for interpreting surface displacements due to shear and tensile faults. The matrix of Okada's formulas (or Green's functions, denoted as G) links the observed surface displacements d to the fault slip distribution m , which can be written simply as $Gm = d$. A Laplacian smoothing operator is used to control the smoothness of the slip model and to prevent instability during the inversion. The optimal smoothing factor for each dataset is determined by the tradeoff curve between the slip roughness and the data misfit, as shown in Supplementary Fig. S3. We then adjust the weighting ratios among the different datasets considering the slip roughness and the fitting of the data to the inversion model. An appropriate smoothing factor is chosen for the joint inversion according to Price and Bürgmann

(2002). The weighting ratios adopted for the leveling, GPS, and InSAR data are 1:2:3. The method of steepest descent (Curry, 1944; Wang et al., 2013) is used for the constrained least-squares inversion.

3. Results

3.1. Coseismic displacements from InSAR data

The original interferograms from the eight ascending tracks of PALSAR data, the estimated IPS of the interferograms, and the interferograms with the IPS removed are shown in Fig. 3(b)–(d). These results illustrate that the ionospheric artifacts caused significant discontinuities between the coseismic displacement interferograms from the different orbital tracks, reflecting the diverse ionospheric conditions under which the different tracks of SAR data were acquired. The ionospheric correction effectively reduces the discontinuities. The descending interferogram (Fig. 3(g)) is less distorted by the ionosphere than the ascending interferogram. One possible reason for this is that the descending SAR images were acquired in the morning (local time approximately 11:35 AM) when activity in the ionosphere was generally more stable than at night (local time approximately 01:05 AM for path 115) (i.e., when the ascending SAR images were acquired) (Liang et al., 2019; Meyer et al., 2016). In practice, the decorrelation of the descending ScanSAR pair is much stronger than that in the ascending Stripmap pair (see data in Table 1). This fact leads to difficulties in removing ionospheric contributions with the range split-spectrum method (Gomba et al., 2016; Liang et al., 2019). Therefore, we do not apply the ionospheric correction to the descending interferogram.

The maximum positive LOS displacement from the ascending interferograms (moving away from the satellite) was approximately 435 cm and occurred at the tip of the Arauco Peninsula (Fig. 4), while the maximum negative LOS displacement from the descending interferogram (moving toward the satellite) was approximately 330 cm and appeared northeast of Constitución.

3.2. Results of slip inversion

Fig. 5(a) shows the fault slip model (Model A) inverted from a combination of leveling, GPS, and original InSAR (both ascending and descending) data, while Fig. 5(b) shows the model (Model B) inverted from the same dataset but with the IPS removed from the InSAR data. The inversion results based on only the InSAR data are also shown in Fig. 6. The seismic moment (M_0), moment magnitude (M_w), average slip, correlation coefficient, and mean residual of each of the models are given in Table 2. The residuals of the ascending InSAR data in Model A and Model B are shown in Supplementary Fig. S6.

The inversion results from Model B are considered the best, as discussed below in the reliability analysis. According to this model, megathrust rupturing occurred at two asperities that are separated by the Biobio submarine canyon. The regions with large slip correlate well with the structure and morphology of the central Chilean margin (Contreras-Reyes et al., 2017). The maximum slip at the northern asperity reached 15.7 m and was located from $34.6^\circ\text{--}35.4^\circ\text{S}$, corresponding to approximately the same area as the rupture zone of the 1928 earthquake (Beck et al., 1998). The maximum slip at the southern asperity was 9.8 m and occurred at the tip of the Arauco Peninsula, approximately overlapping with the northern end of the rupture zone of the 1960 earthquake (Moreno et al., 2009). This is considered a consequence of the viscoelastic relaxation from the 1960 event (Ding and Lin, 2014). The root mean square (RMS) values of the residuals of the leveling, GPS (E/N/U), and ascending and descending InSAR data from the slip inversion are 39.3 cm, 18.5/20.5/17.2 cm, and 9.4 cm and 15.0 cm, respectively. The seismic moment (M_0) from the slip model is 2.29×10^{22} Nm (equivalent to a M_w 8.84 event) by assuming a shear modulus of 40 GPa, and this result is very close to the seismological estimate ($M_0 = 2.26 \times 10^{22}$ Nm and $M_w = 8.84$) (Duputel et al., 2012).

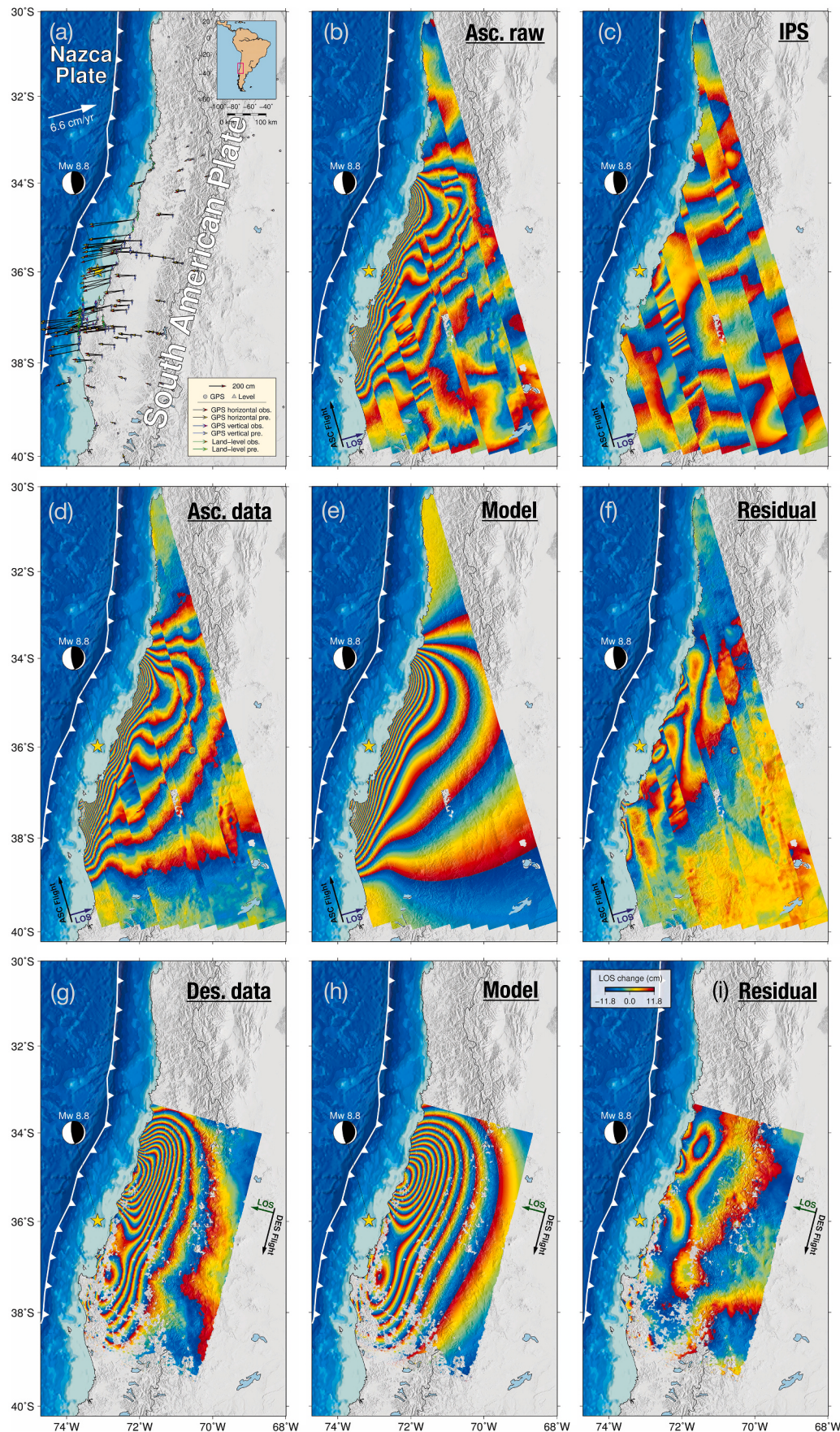


Fig. 3. Coseismic displacements and results of slip inversion. (a) GPS and leveling observations and model prediction (residuals are plotted in Supplementary Fig. S4). (b) Eight tracks of original ascending interferograms. (c) Estimated ionospheric phase screen. (d) Ascending interferograms with the ionospheric phase screen removed. (e) Displacement distribution from inversion model. (f) Difference between (d) and (e). (g) Descending interferogram. (h) Displacement distribution from inversion model. (i) Difference between (g) and (h). All the interferograms are rewrapped. One fringe represents an LOS displacement of 23.6 cm.

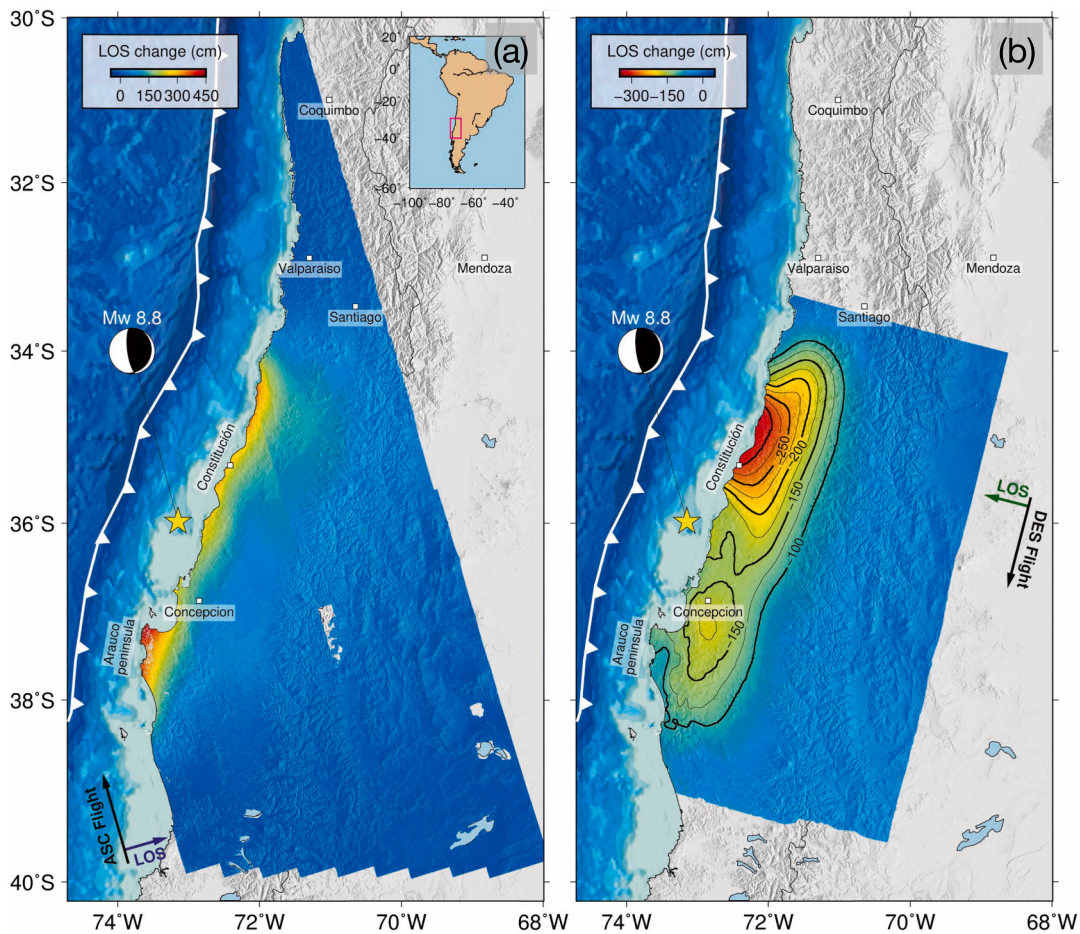


Fig. 4. Line-of-sight displacements from (a) ascending and (b) descending interferograms.

3.3. Reliability analysis

A jackknife resampling technique (Efron and Stein, 1981; Melgar et al., 2015) is implemented to test the reliability of Models A and B. Twenty percent of the downsampled InSAR data are removed randomly (with the other data remaining), and the slip models are regenerated with the remaining data and the same smoothing level as those of the final inversions. The removed data are then returned to the data pool, and the process is repeated by eliminating another 20% of the InSAR data. This is repeated 50 times, and Fig. 7 shows the mean slip values, the standard deviations of the slip, and the variation ratio that is calculated by dividing the mean slip value by the slip value of the chosen model. If the ratio is close to 1, the solution is considered reliable.

The reliability of the model parameters is truly improved after mitigating the ionospheric contributions to InSAR data since the uncertainty of the inverted model parameters is also reduced. Fig. 7 shows that the mean slip magnitudes of Model B are very close to the slip magnitudes of the model (as shown in Fig. 5(b)). The low standard deviation and variation ratio of Model B also demonstrate the high reliability of the model. The high variation ratio in the region enlarged in the circle in Fig. 7(c) further shows the reliability of Model B. It also demonstrates that the increased slip in Model B is highly related to the ionospheric artifacts in InSAR data.

3.4. Analysis of model resolution

The resolution of a model is a function of the observations and the regularization (smoothing) matrix and is independent of the specific data values (Menke, 2012). A model resolution analysis is carried out to

assess the spatial resolving ability of the preferred model, Model B (Supplementary Fig. S7). The model parameters can be fully resolved if the diagonal elements of the resolution matrix are all equal to 1. The spatial resolution varies in the dip direction, as the geodetic data are within the onshore area only, suggesting that the slip along the mid-dip and downdip segments of the fault is well resolved (> 0.5). However, the spatial resolution decreases quickly (< 0.5) starting at a depth of approximately 15 km. The geodetic data provide very few constraints near the trench in general, except for the northern and southern ends of the trench near Constitución ($\sim 35.2^\circ\text{S}$) and the Arauco Peninsula ($\sim 37^\circ\text{S}$), respectively. The shallow fault slip in these two regions is also well resolved (> 0.5 in the south and > 0.4 in the north).

Theoretically, mitigating ionospheric artifacts in the data does not significantly impact the model spatial resolution. When correcting the ionospheric artifacts beforehand is difficult, excluding the InSAR data that are seriously contaminated is the only way to prevent biases in the inversion, as observed in (Tong et al., 2010). In such cases, compared to discarding the data, mitigating the ionospheric artifacts in InSAR data can increase the number of data points in the inversion and can thus improve the model spatial resolution. Nevertheless, the improvement is limited when a large number of effective observations or alternative interferometric pairs are available.

3.5. Comparison with tsunami waveform observations

When large coseismic slip propagates to the uppermost part of an accretionary prism, large seafloor displacements and tsunamis are often produced. Compared with onshore geodetic observations, tsunami waveform observations are particularly susceptible to shallow slip and

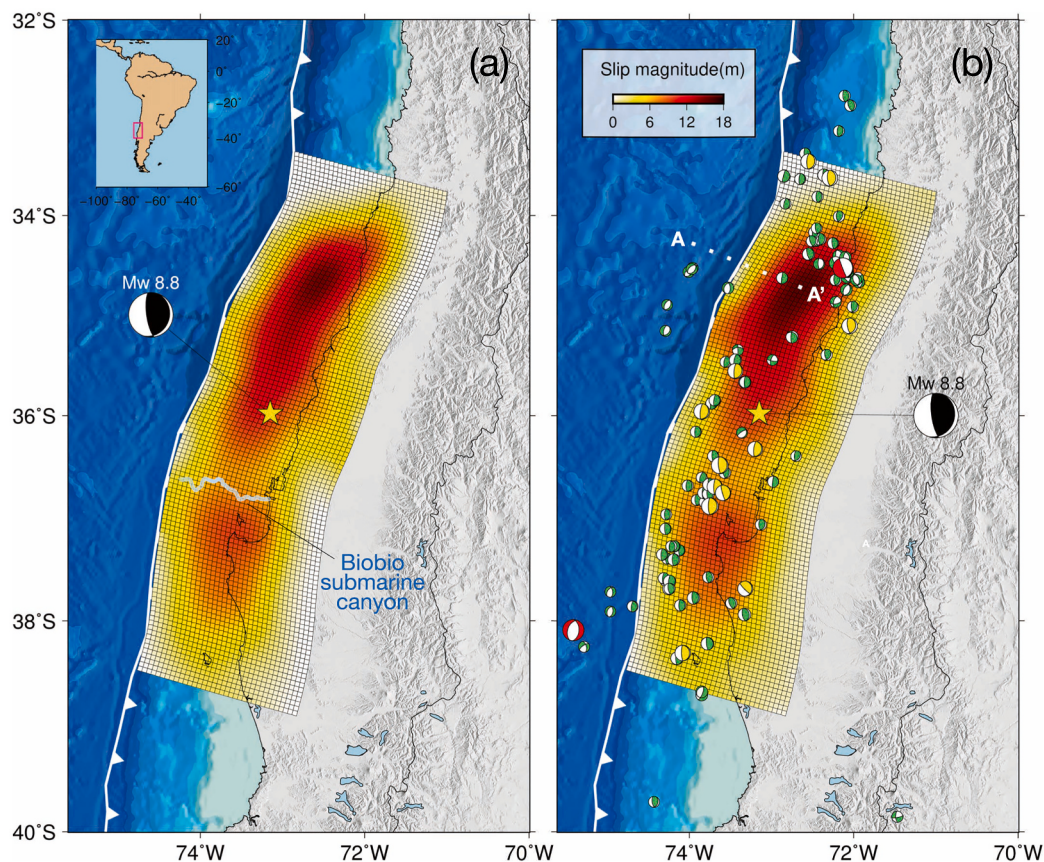


Fig. 5. Fault slip distributions inverted by using joint leveling, GPS, and InSAR data, (a) before and (b) after applying ionospheric corrections to the InSAR data (Models A and B, respectively). Profiles A–A' show where bathymetric observations were taken (Maksymowicz et al., 2017). The fault geometry was obtained from the USGS Slab2.0 model. The fault slip distribution obtained from the USGS Slab1.0 model (Hayes et al., 2012) is given in Supplementary Fig. S5.

provide the best indication of slip along the trench. We therefore perform a tsunami simulation based on our preferred slip model (Model B) to investigate how well the computed and recorded tsunami waveforms agree at four near-field Deep-ocean Assessment and Reporting of Tsunami (DART) buoys (Fig. 8). The tsunami waveform from Model A is also calculated for comparison. The tsunami waveforms are calculated by applying nonlinear shallow water equations incorporating the effects of Boussinesq dispersion, elastic loading, seawater compressibility, and gravitational potential changes in JAGURS (Baba et al., 2017; Baba et al., 2016). To remove short-wavelength patterns from the coseismic displacements, a smoothing filter is applied to calculate the initial water heights from the derived fault slip parameters (Kajiwara, 1963). The effect of horizontal displacements on steep ocean bottom slopes is also considered when calculating seafloor displacements (Tanioka and Satake, 1996). For the bathymetric data, we use a 2 arc-min grid resampled from the ETOPO1 bathymetry data. To allow the wave of a tsunami sufficient time to sweep across DART buoy 43412, the chosen integral time of tsunami propagation is 11 h. Fig. 8 shows the tsunami propagation curves derived from Models A and B.

One of the major differences in the tsunami runup between the two models is that the maximum water height is produced in the right sidelobe of the tsunami propagation path due to the slip of the northern asperity in the trench, as indicated by the white dashed box in Fig. 8. The simulated tsunami waveforms agree well with the tsunami waveform observations at DART buoys 32412, 32411, and 43412.

4. Discussion

4.1. Impact of ionospheric artifacts on estimated coseismic slip distribution

Slip model S1 (see Fig. 6) shows that the northern slip asperity was shifted and that the southern asperity was overestimated due to the presence of ionospheric anomalies. For comparison with the previous solutions (Lorito et al., 2011; Moreno et al., 2012; Pollitz et al., 2011; Tong et al., 2010; Vigny et al., 2011; Yue et al., 2014), we also derive a model (Model S2) based on published ascending InSAR data, e.g., from Tong et al. (2010), as these data have been widely adopted. The solution is improved by excluding data severely affected by ionospheric variation, but it appears that the slip is still underestimated in general, especially at the northern asperity (e.g., at approximately 35°S). A popular strategy has been to exclude data that are seriously affected by ionospheric variation in slip inversions (Feng et al., 2010; Tong et al., 2010).

Model S3 is constructed from the ascending InSAR data after the IPS has been removed. The RMS values of the residuals (Table 2) of Models S1, S2, and S3 are 34.4 cm, 8.4 cm and 5.9 cm, respectively. The descending data constrain the dip-slip motion of the fault well but cannot provide a satisfactory constraint on the strike-slip motion of the fault in this case, as the LOS direction of the descending data is almost perpendicular to the fault line (Model S4).

By combining the ascending and descending InSAR data, we also generate two additional inversion models, one with the removal of the IPS (only for the ascending data) (Model S6) and one without (Model S5). The results show that the slip of Model S6 extends much farther toward the trench than that of Model S5. Removing the ionospheric

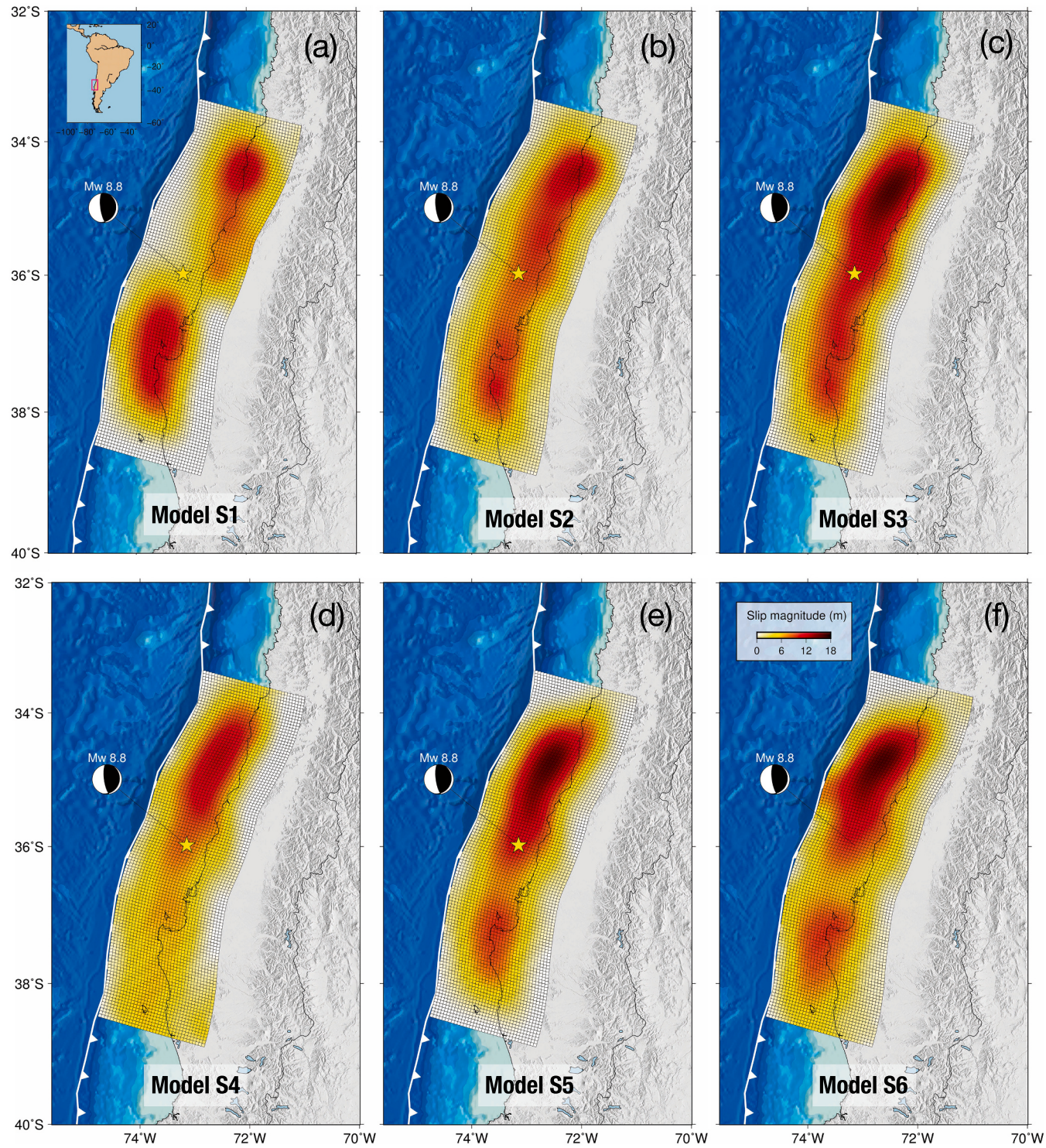


Fig. 6. Fault slip distributions of the 2010 Maule earthquake inverted from InSAR data: (a) ascending InSAR data without IPS correction, (b) ascending InSAR data from Tong et al. (2010), (c) ascending InSAR data after IPS correction, (d) descending InSAR data, (e) ascending and descending InSAR data from Tong et al. (2010), and (f) ascending and descending InSAR data after IPS corrections.

contribution from the ascending InSAR data helps improve the slip magnitude, model fitting, and data residuals.

The results of the joint inversion models, Model A and Model B, resemble those of Model S5 and Model S6. The results from Models B and S6 indicate that only the rupture associated with the northern asperity reached the trench. If the IPS is not removed, the slip inversion results, as shown in Model A and previously published results (Moreno et al., 2012; Tong et al., 2010), do not reflect the slip pattern correctly.

To demonstrate that the difference in the inversion results is not caused by selecting the smoothing factor in the inversion, we plot the results generated using different smoothing factors in Supplementary Fig. S8. The impact of ionospheric artifacts is evident near the northern trench where the model resolution is effectively maintained (> 0.5) (see Supplementary Fig. S7). In addition, tsunami waveform observations are much more sensitive than onshore geodetic data to shallow slip near the trench. As shown in Fig. 8, the tsunami simulations clearly demonstrate

Table 2

Parameters of models presented in Fig. 5 and Fig. 6.

Model	$M_0 (\times 10^{22} \text{ Nm})$	M_w	Peak slip (m)	$R^a (\%)$	Mean RMS residuals (cm)			
					Level	GPS (E/N/U)	Asc. InSAR	Des. InSAR
A	2.16995	8.824 ± 0.003	14.98	93.61	45.0	15.5/19.2/19.1	35.9	14.5
B	2.29245	8.840 ± 0.003	15.74	99.16	39.3	18.5/20.5/17.2	9.4	15.0
S1	1.83210	8.775 ± 0.003	12.72	90.25	—	—	34.4	—
S2	2.14092	8.820 ± 0.003	13.14	99.86	—	—	8.4 ^b	—
S3	2.39029	$8.852^{+0.003}_{-0.002}$	15.84	99.70	—	—	5.9	—
S4	1.89911	8.786 ± 0.003	12.65	99.66	—	—	—	8.1
S5	2.04338	8.807 ± 0.003	15.97	93.33	—	—	37.2	15.3 ^b
S6	2.32675	$8.845^{+0.003}_{-0.004}$	16.05	99.24	—	—	8.5	13.4

^a Correlation coefficient between data and model.^b Published InSAR data from Tong et al. (2010).

that the preferred model (Model B) of slip to the trench near the northern asperity agrees best with the tsunami waveform observations, which provide the most direct indication of slip to the trench. A comparison of the observed tsunami waveform of the first wave arrival (gray shaded regions in Fig. 8) with the simulated tsunami waveforms of Model A and Model B shows that the simulated tsunami waveform improves 47.02% after correcting for the ionospheric contributions to the InSAR data.

The deformation signal may not be affected too much during fault slip inversion when the inverted data are contaminated by random errors. However, ionospheric artifacts are spatially heterogeneous and anisotropic and can be partially explained and resolved by the model. Additionally, if the ionospheric artifacts are independent of the coseismic slip, the residuals of the slip model inverted with the contaminated InSAR data (see Supplementary Fig. S6(a)) would be the same as the estimated ionospheric artifacts (see Fig. 3(c)).

Although this study focuses on a Mw 8.8 earthquake, there are globally many smaller-magnitude earthquakes with a limited spatial scale of displacement. For smaller earthquakes, ionospheric variations dominate InSAR data and are much larger than the deformation. Sophisticated ionospheric correction is still necessary in such cases when ionospheric artifacts are nonnegligible, especially when other types of measurements are limited or not available. This is consistent with the results from our previous study on a Mw 6.6 earthquake in southern Sumatra (Zhang et al., 2018). Ionospheric perturbations are often observed to be associated with megathrust seismic events with larger magnitudes (Galvan et al., 2011; Pulinets, 1998; Tsugawa et al., 2011), especially when the earthquakes are accompanied by tsunamis. Large-scale irregularities and even scintillation in the ionosphere are often present in such cases. Therefore, applying ionospheric corrections to InSAR data is critical for the study of megathrust earthquakes.

In addition to ionospheric artifacts, there are many other error sources that need to be effectively removed from InSAR data, such as orbital, DEM, baseline, phase unwrapping, and tropospheric errors. It is, however, sometimes difficult to make the appropriate corrections to a single image pair, especially when these errors are mixed together. Further studies need to more systematically examine the effects of other InSAR errors on the estimation of the coseismic slip distribution.

4.2. Coseismic rupture

Next, we compare our preferred coseismic slip model with various published results inverted from seismic, tsunami, and geodetic data, as shown in Fig. 9 and Table 3. Our results show that the rupture approached the trench near 34.9°S–35.4°S, with the peak slip reaching 7.2 m. This finding is coincident with the solution of Yue et al. (2014) but different from those of most other studies (Lorito et al., 2011; Moreno et al., 2012; Tong et al., 2010). The peak slip in the results of Yue et al. (2014) extended ~80 km farther along the trench to the north than our results. In contrast to their findings, however, no evidence of

new deformation around the deformation front is detected in the corresponding portion of the northern trench (~34.5°S) based on bathymetric and seismic reflection observations across the trench (Maksymowicz et al., 2017) (Fig. 9(f)). In addition, the slip near the southern trench (~37°S) is smaller (~4.6 m) than that in the north after adapting the fault parameters in the USGS Slab2.0 model. This inconsistency may be due to the difference in slab depth (Hayes et al., 2018). Furthermore, the tsunami simulation based on Model B agrees the best with the observations, especially at the three DART buoys in the north (see Fig. 8).

The rupture of the earthquake may have reached the base of the accretionary prism, the indentation zone in the Mataquito subsegment in the north and the northern edge of the Reloca Slide in the Reloca subsegment in the south (Contreras-Reyes et al., 2010). The frontal accretionary prism (FAP) plays a velocity-strengthening role in subduction earthquakes (Wang and Hu, 2006) and may inhibit ruptures from propagating updip to the trench. The size of the FAP and the backstop position relative to the seismic front are important factors controlling the updip limit in a subduction zone (Contreras-Reyes et al., 2010). According to published seismic profiles (Contreras-Reyes et al., 2017), the size of the FAP near the northern boundary of the trench is 10 km narrower than that in the adjacent areas, and the volume of accreted sediment along the northern segment of the rupture is approximately 26–29% smaller than those in the adjacent segments. Although the seismic front near the southern boundary of the trench is 10–15 km closer landward to the Mataquito subsegment, the volume of the accreted sediment along the Reloca subsegment is approximately twice that along the Mataquito subsegment due to the oversteepening of the lower continental slope (Contreras-Reyes et al., 2016). In addition, irregular structural features, such as seamounts, oceanic ridges, horsts, grabens, and submarine slope failures, have been regarded as factors that may inhibit rupture propagation (Contreras-Reyes et al., 2010; Geersen et al., 2013; Lay et al., 2007; Wang and Hu, 2006). All of these factors may explain the limits of the rupture along the trench, which affected only a relatively small segment of the trench with a length of approximately 65 km.

5. Conclusions

We have estimated for the first time the IPS for some of the SAR interferograms widely used for inverting the source parameters of the 2010 Maule, Chile, earthquake; we have removed the IPS from the interferograms and used the resulting interferograms together with available leveling and GPS data to model the slip distribution. We have found that the coseismic deformation SAR interferograms can be distorted significantly by ionospheric variations, which, if unaccounted for, can subsequently impact the fault slip model derived based on the interferograms. The results have demonstrated that it is critical to analyze and correct for ionospheric effects when InSAR observations are used to study the coseismic displacements of some strong earthquakes (i.e.,

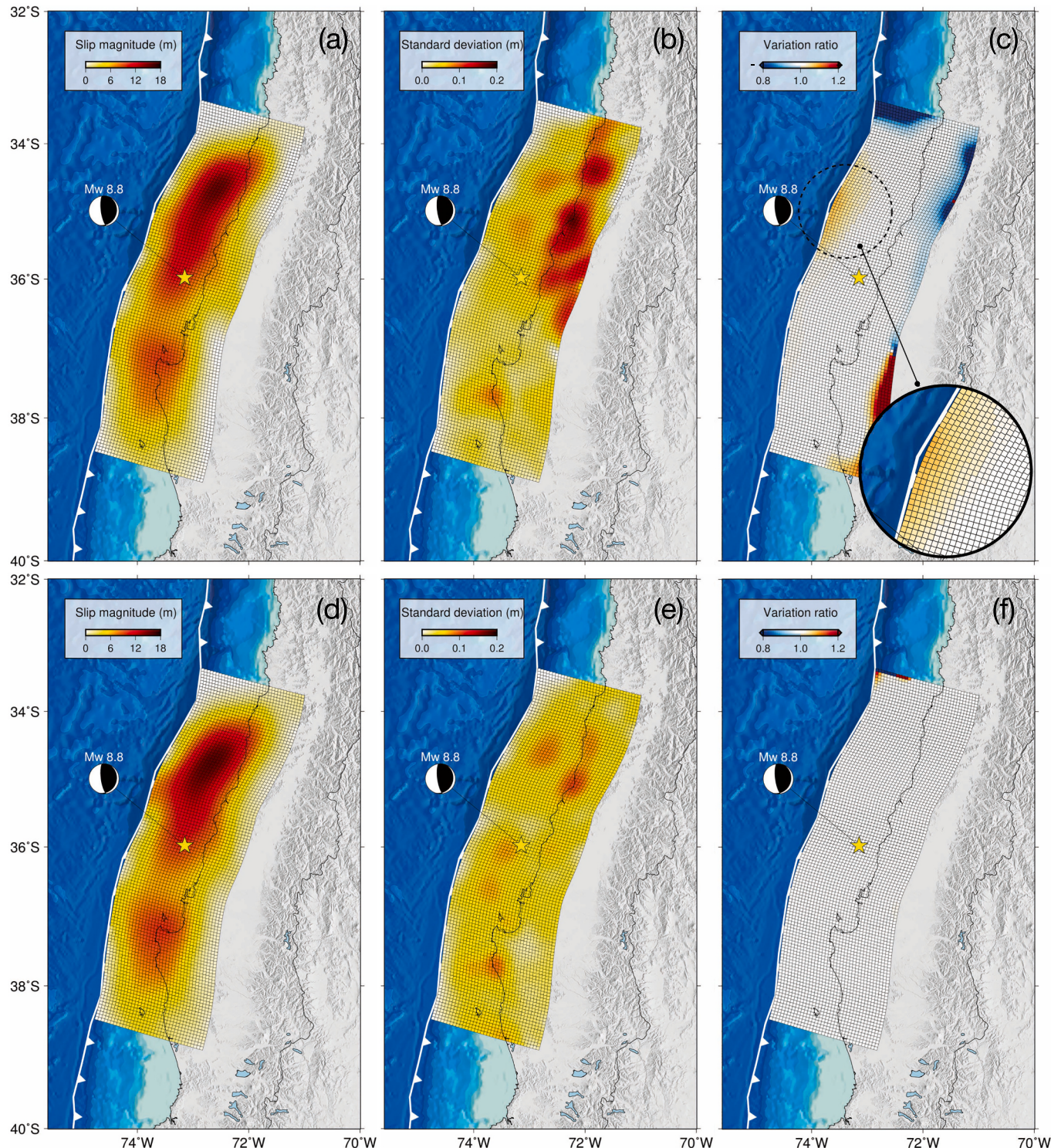


Fig. 7. Results of jackknife sensitivity analyses for Model A (a–c) and Model B (d–e). (a) and (d) are the mean slip magnitudes, (b) and (e) are standard deviations of the slip magnitudes, and (c) and (f) are variation ratios between the mean slip magnitudes and inverted slip magnitude.

megathrust earthquakes), especially when long wavelengths, such as the L-band, SAR data are used. It is therefore advisable at least to check the level of significance of the ionospheric artifacts when studying strong earthquakes with InSAR and to correct for their effects when necessary. The signature of seismic ionospheric perturbation is often presented in such cases, and the ionospheric contribution is nonnegligible compared to the deformation signal in InSAR. We have produced a fault slip model for the earthquake that is considered highly satisfactory, as

demonstrated through cross validation and tsunami simulations. The slip model indicates that the rupture reached the trench only at the northern asperity, a finding that is different from those of most existing research. The findings also explain in part why the existing slip inversion results for the earthquake differ remarkably. The evidence from this study suggests that applying ionospheric corrections to InSAR data helps to reveal fine-scale features in the inverted slip model. The ionospheric phase noise causes both larger-scale and smaller-scale noise in the slip

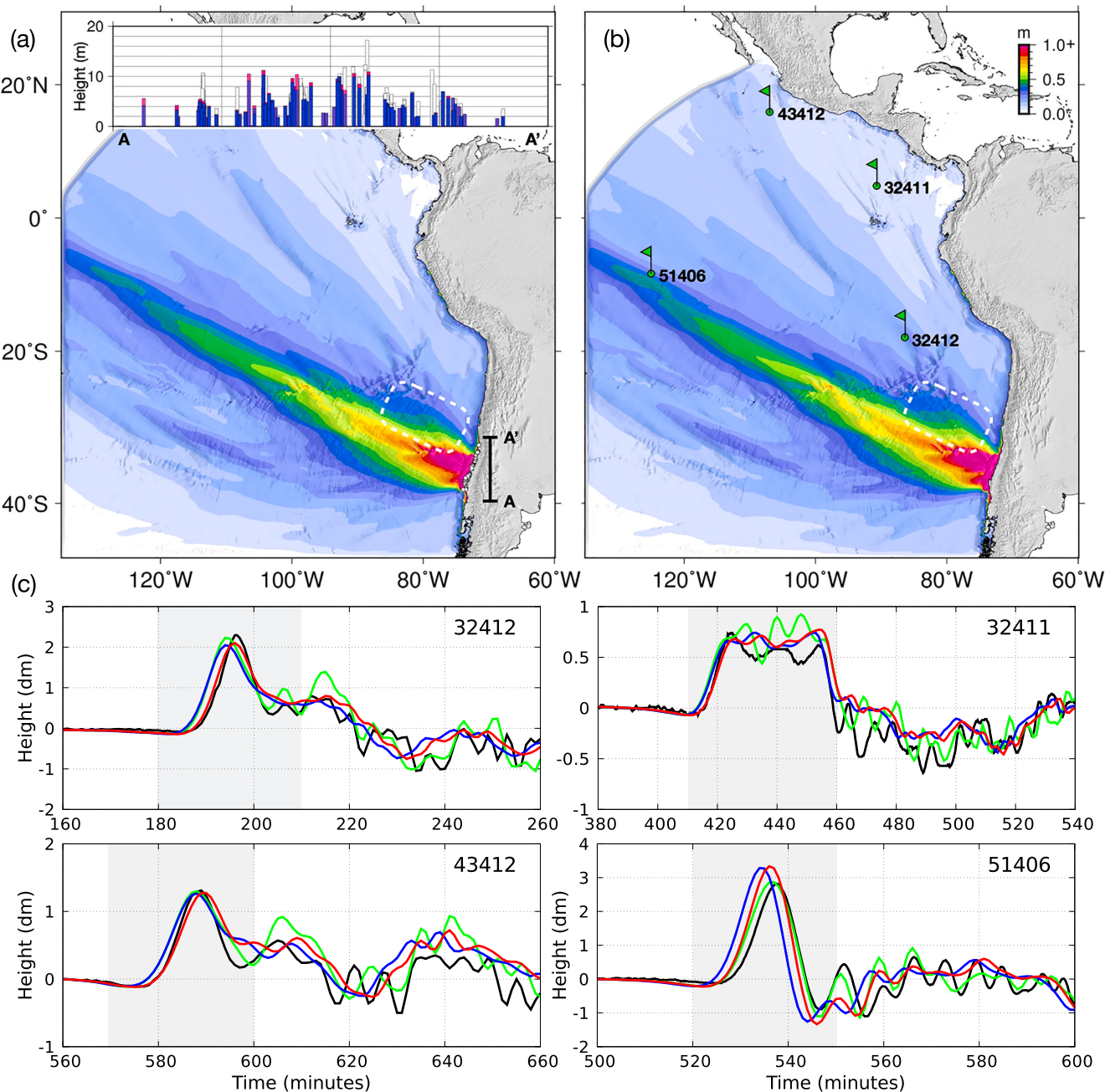


Fig. 8. Tsunami propagation curves derived from Models A and B. (a) and (b) are the maximum wave heights over a period of 11 h for the two models. The inset in (a) compares the runup heights between Model A (blue bars) and Model B (deep pink bars) and the recorded tsunami flow depth (white bars) (Fritz et al., 2011) in the coastal area along A–A'. Green flag signs in (b) indicate the locations of the four near-field Deep-ocean Assessment and Reporting of Tsunami (DART) buoys. (c) Comparisons between the recorded (black line) and runup tsunami waveforms (blue, red, and green lines for Model A, Model B and the model from Yue et al., 2014), respectively at the locations of the four buoys. (For interpretation of the references to colour in this figure legend, the reader is referred to the web version of this article.)

inversion and is dependent on the acquisition time and wavelength of SAR data, geographic location of the earthquake, magnitude of the earthquake, and spatial scale of the earthquake displacement field. Although this study focused on one strong earthquake, a study similar to this one for other earthquakes, even smaller earthquakes, is highly recommended.

Acknowledgments and data

The derived slip models and additional information on the work are available in the supplementary material. This work was supported by

the Research Grants Council of the Hong Kong Special Administrative Region (Projects PolyU 152232/17E, PolyU 152164/18E and PolyU 152233/19E), the Guangdong Basic and Applied Basic Research Foundation (No. 2021A1515011427), the National Natural Science Foundation of China (Grants 41790445 and 41974006), the Shenzhen Scientific Research and Development Funding Program (Nos. 20200807110745001, KQJSCX20180328093453763 and JCYJ20180305125101282), the Department of Education of Guangdong (218KTSCX196), the Fundamental Research Funds for the Central Universities (300102269207) and the Research Institute for Sustainable Urban Development (RISUD) (BBWB). We would like to thank the

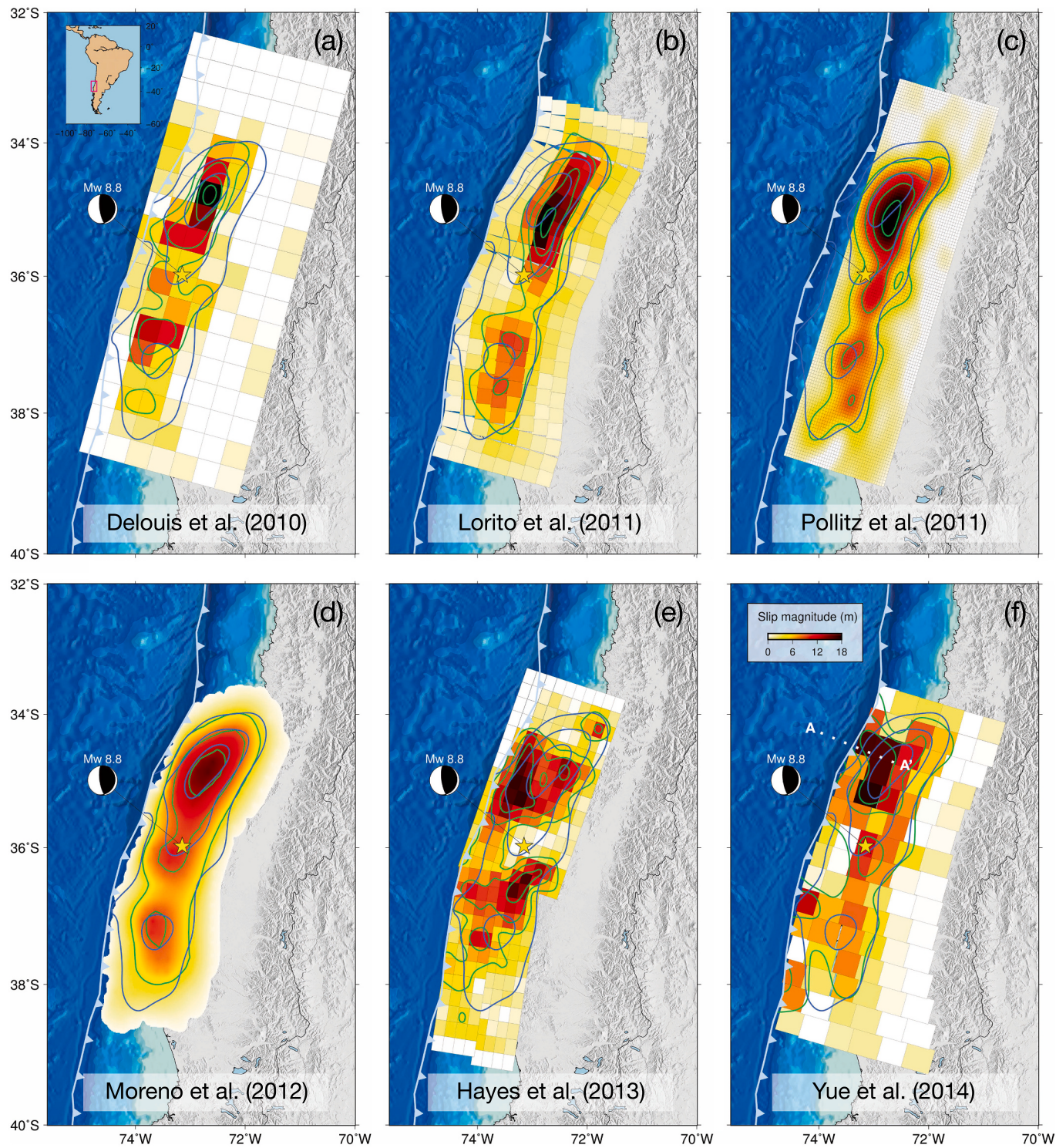


Fig. 9. Comparison between the preferred slip model (Model B) (blue contour lines) and some published fault slip models (green contour lines). The contour interval is 4.5 m. (For interpretation of the references to colour in this figure legend, the reader is referred to the web version of this article.)

reviewers for the constructive comments and Songbo Wu and Hongyu Liang for the valuable discussions. The authors would like to thank the Japan Aerospace Exploration Agency (JAXA) for providing the ALOS PALSAR data under the RA6 PI Projects PI3380 and PI3232. Some of the ALOS PALSAR data were downloaded from the Alaska Satellite Facility (ASF) Distributed Active Archive Center (DAAC) website (<https://vertex.daac.asf.alaska.edu/>) and are copyrighted to JAXA/METI. Some of the published slip models used in the study were downloaded from the SRCMOD database (<http://equake-rc.info/SRCMOD/>). The

tsunami waveform data from DART buoys were obtained from the National Centers for Environmental Information of the U.S. National Ocean and Atmospheric Administration (https://www.ngdc.noaa.gov/hazard/dart/2010chile_dart.html). Some of the figures were generated by Generic Mapping Tools (GMT 5.2.1) software (<http://gmt.soest.hawaii.edu>).

Table 3

Summary of the slip distribution models for the 2010 Maule earthquake.

Study	Peak Slip (m)		Slip extending to Trench?	M_w	$M_o (\times 10^{22} \text{ Nm})$	Fault Geometry	Data used
	North	South					
Lay et al. (2010)	~16	~10	>10 m from trench	8.8	2.1	Planar	seismic data
Delouis et al. (2010)	~21	~13	~4.5 m from northern trench	8.8	1.8	Planar	geodetic ^a and seismic data
Tong et al. (2010)	~17	~10	6–8 m near the trench	8.77	1.82	Planar	geodetic ^a
Lorito et al. (2011)	18–19	9–10	1–4 m near the trench	8.8	1.55	Variable	geodetic ^b , seismic, and tsunami data
Pollitz et al. (2011)	18.8	~9	not evident	8.8	1.97	Planar	geodetic ^a
Vigny et al. (2011)	>15	>15	6–10 m near the trench	8.76	1.76	Variable	geodetic ^b
Moreno et al. (2012)	~16	~10	~5 m from northern trench	8.8	2	Variable	geodetic ^b
Hayes et al. (2013)	~16	~10	6–13 m near the trench	8.9	2.5	Five planes	seismic data
Lin et al. (2013)	~16	<8	not evident	8.8	2.25	Variable	geodetic ^a and seismic data
Yue et al. (2014)	~16	~12	both northern and southern trenches	8.88	2.6	Variable	geodetic ^a , seismic, and tsunami data
This study	15.7	9.8	only northern trench	8.84	2.29	Variable	geodetic ^b

^a Including GPS and InSAR.^b Including land-level, GPS and InSAR.**Declaration of Competing Interest**

The authors declare that they have no known competing financial interests or personal relationships that could have appeared to influence the work reported in this paper.

Appendix A. Supplementary data

Supplementary data to this article can be found online at <https://doi.org/10.1016/j.rse.2021.112733>.

References

- Baba, T., Ando, K., Matsuoka, D., Hyodo, M., Hori, T., Takahashi, N., Obayashi, R., Imato, Y., Kitamura, D., Uehara, H., 2016. Large-scale, high-speed tsunami prediction for the Great Nankai Trough earthquake on the K computer. *Int. J. High Perform. Comput. Appl.* 30, 71–84.
- Baba, T., Allgeyer, S., Hossen, J., Cummins, P.R., Tsushima, H., Imai, K., Yamashita, K., Kato, T., 2017. Accurate numerical simulation of the far-field tsunami caused by the 2011 Tohoku earthquake, including the effects of Boussinesq dispersion, seawater density stratification, elastic loading, and gravitational potential change. *Ocean Model.* 111, 46–54.
- Bamler, R., Eineder, M., 1996. ScanSAR processing using standard high precision SAR algorithms. *IEEE Trans. Geosci. Remote Sens.* 34, 212–218.
- Barbot, S., Hamel, Y., Fialko, Y., 2008. Space geodetic investigation of the coseismic and postseismic deformation due to the 2003 Mw7.2 Altai earthquake: implications for the local lithospheric rheology. *J. Geophys. Res. Solid Earth* 113.
- Bechor, N.B.D., Zebker, H.A., 2006. Measuring two-dimensional movements using a single InSAR pair. *Geophys. Res. Lett.* 33, L16311.
- Beck, S., Barrientos, S., Kausel, E., Reyes, M., 1998. Source characteristics of historic earthquakes along the central Chile subduction Askew et Alzone. *J. S. Am. Earth Sci.* 11, 115–129.
- Bird, P., 2003. An updated digital model of plate boundaries. *Geochem. Geophys. Geosyst.* 4.
- Campos, J., Hatzfeld, D., Madariaga, R., Lopez, G., Kausel, E., Zollo, A., Iannaccone, G., Fromm, R., Barrientos, S., Lyon-Caen, H., 2002. A seismological study of the 1835 seismic gap in south-central Chile. *Phys. Earth Planet. Inter.* 132, 177–195.
- Chen, C.W., Zebker, H.A., 2001. Two-dimensional phase unwrapping with use of statistical models for cost functions in nonlinear optimization. *JOSA A* 18, 338–351.
- Chen, A.C., Zebker, H.A., 2014. Reducing ionospheric effects in InSAR data using accurate coregistration. *IEEE Trans. Geosci. Remote Sens.* 52, 60–70.
- Contreras-Reyes, E., Flueh, E.R., Grevemeyer, I., 2010. Tectonic control on sediment accretion and subduction off south Central Chile: implications for coseismic rupture processes of the 1960 and 2010 megathrust earthquakes. *Tectonics* 29.
- Contreras-Reyes, E., Völker, D., Bialas, J., Moscoso, E., Grevemeyer, I., 2016. Reloca slide: an ~24 km³ submarine mass-wasting event in response to over-steepening and failure of the central Chilean continental slope. *Terra Nova* 28, 257–264.
- Contreras-Reyes, E., Maksymowicz, A., Lange, D., Grevemeyer, I., Muñoz-Linfold, P., Moscoso, E., 2017. On the relationship between structure, morphology and large coseismic slip: a case study of the M w 8.8 Maule, Chile 2010 earthquake. *Earth Planet. Sci. Lett.* 478, 27–39.
- Cumming, I.G., Wong, F.H., 2005. Digital Processing of Synthetic Aperture Radar Data (Artech house).
- Curry, H.B., 1944. The method of steepest descent for non-linear minimization problems. *Q. Appl. Math.* 2, 258–261.
- Delouis, B., Nocquet, J.M., Vallée, M., 2010. Slip distribution of the February 27, 2010 Mw= 8.8 Maule earthquake, central Chile, from static and high-rate GPS, InSAR, and broadband teleseismic data. *Geophys. Res. Lett.* 37 (17).
- Ding, M., Lin, J., 2014. Post-seismic viscoelastic deformation and stress transfer after the 1960 M 9.5 Valdivia, Chile earthquake: effects on the 2010 M 8.8 Maule, Chile earthquake. *Geophys. J. Int.* 197, 697–704.
- Ding, X., Li, Z., Zhu, J., Feng, G., Long, J., 2008. Atmospheric effects on InSAR measurements and their mitigation. *Sensors* 8, 5426–5448.
- Duputel, Z., Rivera, L., Kanamori, H., Hayes, G., 2012. W phase source inversion for moderate to large earthquakes (1990–2010). *Geophys. J. Int.* 189, 1125–1147.
- Efron, B., Stein, C., 1981. The jackknife estimate of variance. *Ann. Stat.* 586–596.
- Farías, M., Vargas, G., Tassara, A., Carretero, S., Baize, S., Melnick, D., Bataille, K., 2010. Land-level changes produced by the Mw 8.8 2010 Chilean earthquake. *Science* 329, 916.
- Farr, T.G., Kobrick, M., 2000. Shuttle radar topography mission produces a wealth of data. *EOS Trans. Am. Geophys. Union* 81, 583–585.
- Fattah, H., Simons, M., Agram, P., 2017. InSAR time-series estimation of the ionospheric phase delay: an extension of the split range-spectrum technique. *IEEE Trans. Geosci. Remote Sens.* 55, 5984–5996.
- Feng, G., Jónsson, S., 2012. Shortcomings of InSAR for studying megathrust earthquakes: the case of the Mw9.0 Tohoku-Oki earthquake. *Geophys. Res. Lett.* 39.
- Feng, G., Hetland, E.A., Ding, X., Li, Z., Zhang, L., 2010. Coseismic fault slip of the 2008 Mw 7.9 Wenchuan earthquake estimated from InSAR and GPS measurements. *Geophys. Res. Lett.* 37 no. L01302.
- Fritz, H.M., Petroff, C.M., Catalán, P.A., Cienfuegos, R., Winckler, P., Kalligeris, N., Weiss, R., Barrientos, S.E., Meneses, G., Valderas-Bermejo, C., Ebeling, C., Papadopoulos, A., Contreras, M., Almar, R., Dominguez, J.C., Synolakis, C.E., 2011. Field survey of the 27 February 2010 Chile tsunami. *Pure Appl. Geophys.* 168 (11), 1989–2010.
- Galvan, D.A., Komjathy, A., Hickey, M.P., Mannucci, A.J., 2011. The 2009 Samoa and 2010 Chile tsunamis as observed in the ionosphere using GPS total electron content. *J. Geophys. Res. Space Physics* 116.
- Geersen, J., Völker, D., Behrmann, J.H., Kläschen, D., Weinrebe, W., Krastel, S., Reichert, C., 2013. Seismic rupture during the 1960 Great Chile and the 2010 Maule earthquakes limited by a giant Pleistocene submarine slope failure. *Terra Nova* 25, 472–477.
- Goldstein, R.M., Werner, C.L., 1998. Radar interferogram filtering for geophysical applications. *Geophys. Res. Lett.* 25, 4035–4038.
- Gombá, G., Parizzi, A., De Zan, F., Eineder, M., Bamler, R., 2016. Toward operational compensation of ionospheric effects in SAR interferograms: the split-spectrum method. *IEEE Trans. Geosci. Remote Sens.* 54, 1446–1461.
- Gray, A.L., Mattar, K.E., Sofko, G., 2000. Influence of ionospheric electron density fluctuations on satellite radar interferometry. *Geophys. Res. Lett.* 27, 1451–1454.
- Hayes, G.P., Wald, D.J., Johnson, R.L., 2012. Slab1.0: a three-dimensional model of global subduction zone geometries. *J. Geophys. Res. Solid Earth* 117 (B1).
- Hayes, G.P., Bergman, E., Johnson, K.L., Benz, H.M., Brown, L., Meltzer, A.S., 2013. Seismotectonic framework of the 2010 February 27 M w 8.8 Maule, Chile earthquake sequence. *Geophys. J. Int.* 195, 1034–1051.
- Hayes, G.P., Herman, M.W., Barnhart, W.D., Furlong, K.P., Riquelme, S., Benz, H.M., Bergman, E., Barrientos, S., Earle, P.S., Samsonov, S., 2014. Continuing megathrust earthquake potential in Chile after the 2014 Iquique earthquake. *Nature* 512, 295.
- Hayes, G.P., Moore, G.L., Portner, D.E., Hearne, M., Flamme, H., Furtney, M., Smoczyk, G.M., 2018. Slab2, a comprehensive subduction zone geometry model. *Science* 362, 58–61.
- Jung, H.-S., Won, J.-S., Kim, S.-W., 2009. An improvement of the performance of multiple-aperture SAR interferometry (MAI). *IEEE Trans. Geosci. Remote Sens.* 47, 2859–2869.
- Kajirawa, K., 1963. The leading wave of the tsunami. *Bull. Earthquake Res. Inst. Tokyo Univ.* 4 (3), 535–571.
- Lay, T., Bilek, S., Dixon, T., Moore, C., 2007. Anomalous earthquake ruptures at shallow depths on subduction zone megathrusts. In: The Seismogenic Zone of Subduction Thrust Faults, pp. 476–511.
- Lay, T., Ammon, C., Kanamori, H., Koper, K., Sufri, O., Hutko, A., 2010. Teleseismic inversion for rupture process of the 27 February 2010 Chile (Mw 8.8) earthquake. *Geophys. Res. Lett.* 37.

- Leys, C., Ley, C., Klein, O., Bernard, P., Licata, L., 2013. Detecting outliers: do not use standard deviation around the mean, use absolute deviation around the median. *J. Exp. Soc. Psychol.* 49, 764–766.
- Liang, H., Zhang, L., Ding, X., Lu, Z., Li, X., 2018. Toward mitigating stratified tropospheric delays in multitemporal InSAR: a Quadtree aided joint model. *IEEE Trans. Geosci. Remote Sens.* 57 (1), 291–303.
- Liang, C., Agram, P., Simons, M., Fielding, E.J., 2019. Ionospheric correction of insar time series analysis of c-band sentinel-1 tops data. *IEEE Trans. Geosci. Remote Sens.* 57, 6755–6773.
- Lin, Y.N., Sladen, A., Ortega-Culaciati, F., Simons, M., Avouac, J.P., Fielding, E.J., Brooks, B.A., Bevis, M., Genrich, J., Rietbrock, A., 2013. Coseismic and postseismic slip associated with the 2010 Maule earthquake, Chile: characterizing the Arauco Peninsula barrier effect. *J. Geophys. Res. Solid Earth* 118, 3142–3159.
- Lorito, S., Romano, F., Atzori, S., Tong, X., Avallone, A., McCloskey, J., Cocco, M., Boschi, E., Piatanesi, A., 2011. Limited overlap between the seismic gap and coseismic slip of the great 2010 Chile earthquake. *Nat. Geosci.* 4, 173.
- Maksymowicz, A., Chadwell, C., Ruiz, J., Tréhu, A., Contreras-Reyes, E., Weinrebe, W., Díaz-Naveas, J., Gibson, J., Lonsdale, P., Tryon, M., 2017. Coseismic seafloor deformation in the trench region during the Mw8.8 Maule megathrust earthquake. *Sci. Rep.* 7, 45918.
- Melgar, D., Geng, J., Crowell, B.W., Haase, J.S., Bock, Y., Hammond, W.C., Allen, R.M., 2015. Seismogeodesy of the 2014 Mw6.1 Napa earthquake, California: rapid response and modeling of fast rupture on a dipping strike-slip fault. *J. Geophys. Res. Solid Earth* 120, 5013–5033.
- Menke, W., 2012. *Geophysical Data Analysis: Discrete Inverse Theory*, Third ed. Academic Press.
- Meyer, F., Bamler, R., Jakowski, N., Fritz, T., 2006. The potential of low-frequency SAR systems for mapping ionospheric TEC distributions. *IEEE Geosci. Remote Sens. Lett.* 3, 560–564.
- Meyer, F.J., Chotoo, K., Chotoo, S.D., Huxtable, B.D., Carrano, C.S., 2016. The influence of equatorial scintillation on L-band SAR image quality and phase. *IEEE Trans. Geosci. Remote Sens.* 54, 869–880.
- Moreno, M.S., Bolte, J., Klotz, J., Melnick, D., 2009. Impact of megathrust geometry on inversion of coseismic slip from geodetic data: application to the 1960 Chile earthquake. *Geophys. Res. Lett.* 36.
- Moreno, M., Rosenau, M., Oncken, O., 2010. 2010 Maule earthquake slip correlates with pre-seismic locking of Andean subduction zone. *Nature* 467 (7312), 198–202.
- Moreno, M., Melnick, D., Rosenau, M., Baez, J., Klotz, J., Oncken, O., Tassara, A., Chen, J., Bataille, K., Bevis, M., 2012. Toward understanding tectonic control on the Mw 8.8 2010 Maule Chile earthquake. *Earth Planet. Sci. Lett.* 321, 152–165.
- Okada, Y., 1985. Surface deformation due to shear and tensile faults in a half-space. *Bull. Seismol. Soc. Am.* 75 (4), 1135–1154.
- Pollitz, F.F., Brooks, B., Tong, X., Bevis, M.G., Foster, J.H., Bürgmann, R., Smalley, R., Vigny, C., Socquet, A., Ruegg, J.C., 2011. Coseismic slip distribution of the February 27, 2010 Mw 8.8 Maule, Chile earthquake. *Geophys. Res. Lett.* 38.
- Price, E.J., Bürgmann, R., 2002. Interactions between the Landers and Hector Mine, California, earthquakes from space geodesy, boundary element modeling, and time-dependent friction. *Bull. Seismol. Soc. Am.* 92, 1450–1469.
- Pulinets, S., 1998. Seismic activity as a source of the ionospheric variability. *Adv. Space Res.* 22, 903–906.
- Rosen, P., Hensley, S., Chen, C., 2010. Measurement and mitigation of the ionosphere in L-band Interferometric SAR data. In: 2010 IEEE Radar Conference 2010, pp. 1459–1463.
- Scott, C.P., Lohman, R.B., 2016. Sensitivity of earthquake source inversions to atmospheric noise and corrections of InSAR data. *J. Geophys. Res. Solid Earth* 121, 4031–4044.
- Shimada, M., Ohtaki, T., 2010. Generating large-scale high-quality SAR mosaic datasets: application to PALSAR data for global monitoring. *IEEE J. Select. Top. Appl. Earth Observ. Remote Sens.* 3, 637–656.
- Tanioka, Y., Satake, K., 1996. Tsunami generation by horizontal displacement of ocean bottom. *Geophys. Res. Lett.* 23, 861–864.
- Tong, X., Sandwell, D., Luttrell, K., Brooks, B., Bevis, M., Shimada, M., Foster, J., Smalley, R., Parra, H., Báez Soto, J.C., 2010. The 2010 Maule, Chile earthquake: downdip rupture limit revealed by space geodesy. *Geophys. Res. Lett.* 37.
- Tsugawa, T., Saito, A., Otsuka, Y., Nishioka, M., Maruyama, T., Kato, H., Nagatsuka, T., Murata, K.T., 2011. Ionospheric disturbances detected by GPS total electron content observation after the 2011 off the Pacific coast of Tohoku Earthquake. *Earth Planet Space* 63, 66.
- Vigny, C., Socquet, A., Peyrat, S., Ruegg, J.-C., Métois, M., Madariaga, R., Morvan, S., Lancieri, M., Lacassin, R., Campos, J., 2011. The 2010 Mw 8.8 Maule megathrust earthquake of central Chile, monitored by GPS. *Science* 332, 1417–1421.
- Wang, K., Fialko, Y., 2018. Observations and modeling of coseismic and postseismic deformation due to the 2015 Mw 7.8 Gorkha (Nepal) earthquake. *J. Geophys. Res. Solid Earth* 123, 761–779.
- Wang, K., Hu, Y., 2006. Accretionary prisms in subduction earthquake cycles: the theory of dynamic Coulomb wedge. *J. Geophys. Res. Solid Earth* 111 (B6).
- Wang, R., Diao, F., Hoechner, A., 2013. SDM-A geodetic inversion code incorporating with layered crust structure and curved fault geometry. In: EGU General Assembly Conference Abstracts, 15, pp. EGU2013–2411.
- Xu, W., 2017. Finite-fault slip model of the 2016 Mw 7.5 Chiloé earthquake, Southern Chile, estimated from Sentinel-1 data. *Geophys. Res. Lett.* 44, 4774–4780.
- Xu, Z.-W., Wu, J., Wu, Z.-S., 2004. A survey of ionospheric effects on space-based radar. *Wave Random Media* 14, S189–S273.
- Yu, C., Li, Z., Penna, N.T., 2018. Interferometric synthetic aperture radar atmospheric correction using a GPS-based iterative tropospheric decomposition model. *Remote Sens. Environ.* 204, 109–121.
- Yue, H., Lay, T., Rivera, L., An, C., Vigny, C., Tong, X., Báez Soto, J.C., 2014. Localized fault slip to the trench in the 2010 Maule, Chile Mw= 8.8 earthquake from joint inversion of high-rate GPS, telesismic body waves, InSAR, campaign GPS, and tsunami observations. *J. Geophys. Res. Solid Earth* 119, 7786–7804.
- Zhang, B., Ding, X., Zhu, W., Wang, C., Zhang, L., Liu, Z., 2016. Mitigating ionospheric artifacts in coseismic interferogram based on offset field derived from ALOS-PALSAR data. *IEEE J. Select. Top. Appl. Earth Observ. Remote Sens.* 9, 3050–3059.
- Zhang, B., Wang, C., Ding, X., Zhu, W., Wu, S., 2018. Correction of ionospheric artifacts in SAR data: application to fault slip inversion of 2009 southern Sumatra earthquake. *IEEE Geosci. Remote Sens. Lett.* 15, 1327–1331.